JOURNAL OF SPACECRAFT AND ROCKETS
Vol. 48, No. 2, March–April 2011

Fully-Propulsive Mars Atmospheric Transit Strategies for High-Mass Missions

Christopher L. Marsh* and Robert D. Braun†
Georgia Institute of Technology, Atlanta, Georgia 30332

DOI: 10.2514/1.49394

A systems analysis focused on the use of propulsion throughout the entry, descent, and landing sequence at Mars for high-payload missions is presented. Trajectory simulation and mass sizing are performed to analyze the feasibility of a fully-propulsive descent. A heat rate boundary and associated control law are developed in an effort to limit the heat rate encountered by the vehicle. Analysis is performed to explore the full-propulsive entry, descent, and landing strategy's sensitivity to the vehicle's propulsive capabilities and aeropropulsive and vehicle models. The strategy is examined across a range of initial masses and heat rate constraints, outlining an envelope of feasibility. The proposed architecture is compared against traditional Mars entry, descent, and landing systems in which significant aeroassist technology is employed. With this information, a systematic overview of the impact of a fully-propulsive system on spacecraft design and functionality is offered.

Nomenclature

A	=	reference area, m^2
C_T	=	thrust coefficient
D	=	drag, N
g_0	=	Earth gravitational acceleration, m/s^2
h	=	altitude, m
I_{sp}	=	specific impulse, s
k_{C_D}	=	drag coefficient multiplier
$k_{structure}$	=	structural mass multiplier
$\dot{m}$	=	time derivative of mass, kg/s
$m_{backshell}$	=	backshell mass, kg
m_{engine}	=	engine mass, kg
m_{FBS}	=	forebody structure mass, kg
m_{landed}	=	landed mass, kg
$m_{payload}$	=	payload mass, kg
$m_{prop\ sys}$	=	propellant system mass, kg
$m_{RCS\ sys}$	=	reaction control system mass, kg
m_{TPS}	=	thermal protection system mass, kg
$\bar{q}$	=	dynamic pressure, Pa
$\dot{q}_{conv}$	=	convective heat rate, W/cm^2
$q_{conv,total}$	=	integrated convective heat load, J/cm^2
$\bar{q}_{max}$	=	maximum dynamic pressure, Pa
r_n	=	vehicle nose radius, m
T_{max}	=	maximum thrust, N
T/W	=	thrust-to-weight
V	=	velocity, m/s
$V_{rel,con}$	=	constraint relative velocity, m/s
v_{rel}	=	planet relative velocity, m/s^2
ΔV	=	change in velocity, km/s^2
ε	=	emissivity
ρ	=	atmospheric density, kg/m^3

I. Introduction

THE United States has safely landed six spacecraft on Mars starting with Viking 1 and 2 in 1976 and continuing to the recently landed Phoenix. However, the largest landed mass of these missions is 590 kg [1]. While NASA is currently preparing for flight of the Mars Science Laboratory and its near one metric ton landed payload [2], the Vision for Space Exploration calls for eventually sending humans to Mars with landed payloads in range of 40 to 80 metric tons [3]. One of the most significant challenges of a human Mars mission is in the area of entry, descent, and landing (EDL). Because of the presence of a thin but significant atmosphere at Mars, current Mars EDL strategies and technologies depend heavily on aerodynamic forces to slow the vehicle. These concepts are largely derived from Viking and Earth-return experience. However, this proven approach does not allow for extension of landed mass capability to the level required for human exploration without a significant technology development program [1]. As an example, NASA's previous Design Reference Mission [4] required a cluster of three 50-m-diam Viking heritage parachutes to be deployed supersonically. Such an approach has not been proven in relevant environmental conditions.

The presence of an atmosphere at Mars has influenced Mars EDL architectures to take the form of Earth-return missions using various aeroassist technologies including heat shields, lifting aeroshell configurations, and parachutes. However, the low density of the Mars atmosphere (approximately $\frac{1}{100}$th as dense as Earth's) significantly reduces the effectiveness of these systems. Therefore, a Mars landing architecture comparable to that used in human exploration of the Moon is a natural consideration. In the Apollo program, propulsion was employed in the descent and landing sequence, where the lunar landers' propulsion system provided all of the ΔV required from lunar orbit to landing (more than 2 km/s). Although not the main ΔV contributor in the EDL system, propulsion has been used in several robotic missions to Mars. A summary of the use of propulsion in the lunar and Mars landings is given in Table 1 [1,5–15]. The capabilities required by human Mars exploration greatly surpass those outlined in Table 1.

This paper investigates the ability to employ a fully-propulsive atmospheric transit strategy at Mars for high-mass payload missions. The objective of this systems analysis effort is to provide a fully-propulsive reference architecture for comparison with EDL architectures that employ aeroassist technology. In this study, fully-propulsive descent refers to deceleration sequences that do not include aeroassist technology elements such as lifting aeroshell configurations, ablative thermal protection systems (TPSs), parachutes, or inflatable aerodynamic decelerators (IADs). Instead, these architectures consist of powered flight from Mars orbit or hyperbolic approach conditions to the surface in which deceleration is achieved through a combination of propulsive thrust and aerodynamic drag. The study explores the effect of heat rate constraints on the system

Received 16 February 2010; revision received 1 October 2010; accepted for publication 1 October 2010.

*Lieutenant Junior Grade, United States Navy.
†Associate Professor, Daniel Guggenheim School of Aerospace Engineering. Fellow AIAA.

Table 1 Historic uses of propulsion in EDL [1,5–15]

Mission	Use of propulsion	Propellant type	ΔV imparted, m/s	Maximum thrust, kN	Throttling	I_{sp}, s	Total mass of engines, kg	Mass of propellant, kg	PMF, %	Landed mass, kg
Apollo	Lunar deorbit and landing	N_2O_4/A-50	2010	43.9	10–60% of T_{max}	311	113	8165	49.7–53.8	7000–8250
Viking 1/2	Terminal descent	Hydrazine	220	8.0	10:1	210	23	185	18.6	590
Mars Pathfinder	Terminal descent and flyaway	Solid rockets	63	23.8	None	260	30.7	20.7	3.5	360
Mars Exploration Rover A/B	Terminal descent and flyaway	Solid rockets	57.4/61.8	23.3	None	273.9	17.5	27.1	3.3	539
Phoenix	Terminal descent	Hydrazine	55.3	30.3	Off-pulsed	212.5	30	37.4	6.2	382
Mars Science Laboratory	Terminal descent and flyaway	Hydrazine	120	24	13–100% of T_{max}	210	72	340	11.6	900

design by altering the vehicle's deceleration profile. Propulsive strategies considered include a constant-thrust gravity turn as well as variable thrust trajectory designs. This study examines the fully-propulsive architecture requirements as well as the architecture's sensitivities. Analysis of the fully-propulsive descent strategy is assessed for incorporation into a future, high-mass mission architecture.

II. Approach

A. Simulation

To perform the necessary studies, a MATLAB-based entry simulation was created to propagate the three-degree-of-freedom translational equations of motion from a given set of initial conditions until termination at the surface of the planet. The simulation models a spherical, rotating planet with forces due to gravity, thrust, and drag. The vehicle follows a ballistic trajectory and does not take advantage of aerodynamic lift. The vehicle used in the study is a 70° sphere-cone similar to that used by the robotic missions referenced in Table 1. The simulation uses a tabulated coefficient of drag as a function of Mach number and interpolates between data points. The reference atmosphere used is tabulated from the Mars Pathfinder mission [9]. The calculations used in this study do not include margins on ideal velocities, propulsion performance, or modeled masses.

Simulation validation is critical to ensure the accuracy of the results of this study. As such, a Mars Pathfinder simulation was compared against a trajectory of the same mission simulated with the Program to Optimize Simulated Trajectories (POST) [16]. As shown in Table 2, the trajectory generated by the MATLAB entry simulation is in excellent agreement with the POST trajectory. Position, velocity, flight path angle (FPA), dynamic pressure, heating, and g-load calculations were validated through this process.

The simulator has the ability to use various thrust control modules. These modules specify the thrust direction and magnitude throughout the trajectory. The thrust control module and the mass impact of the use of thrust were validated against an independent simulation used in a recent assessment of Mars pinpoint landing performance [17]. A Newton-based solver is used within the simulator to calculate the altitude at which to begin the constant-thrust gravity turn as to ensure a velocity of less than 0.1 m/s at landing. Table 3 shows excellent agreement between trajectory parameters for the constant-thrust gravity turn validation case.

Table 2 Event comparison for trajectory validation

Event	This study	POST	Difference, %
Entry			
Time, s	0	0	0.00
Altitude, m	128000	128000	0.00
Relative velocity, m/s	7479	7479	−0.01
Relative FPA, deg	−13.65	−13.65	0.00
Parachute deploy			
Time, s	154.5	154.5	0.00
Altitude, m	9916	9916	0.00
Relative velocity, m/s	414.5	414.5	0.01
Relative FPA, deg	−23.35	−23.35	−0.01
Dynamic pressure, Pa	585.0	585.0	0.00
Heat shield jettison			
Time, s	174.5	174.5	0.00
Altitude, m	8217	8219	−0.03
Relative velocity, m/s	90.36	90.23	0.14
Relative FPA, deg	−47.29	−47.33	−0.08
Dynamic pressure, Pa	32.07	31.98	0.30
Trajectory termination			
Time, s	359.8	359.8	0.01
Altitude, m	−2408	−2408	0.00
Relative velocity, m/s	42.64	42.64	0.01
Relative FPA, deg	−89.88	−89.88	0.00
Dynamic pressure, Pa	21.55	21.55	−0.02

Table 3 Event comparison for propulsive maneuver validation

Event	This study	Independent simulation [17]	Difference
Ignition			
Time, s	0.00	0.00	0.00
Mass, kg	9713.24	9713.24	0.00
Altitude, m	14885.40	14885.40	0.00
Relative velocity, m/s	1902.73	1902.73	0.00
Relative FPA, deg	−6.38	−6.38	0.00
Trajectory termination			
Time, s	95.36	95.36	0.00
Mass, kg	6615.61	6615.71	0.10
Altitude, m	0.00	0.17	0.17
Relative velocity, m/s	0.07	0.10	0.03
Relative FPA, deg	−82.36	−81.41	0.95

B. Modeling

Throughout the study, vehicle performance is based largely on the ability to deliver payload to the Mars surface. Vehicle mass modeling is a crucial aspect of the study. The vehicle's initial mass is broken into four general categories: propulsion and reaction control systems (RCSs), TPS, structure, and payload. A majority of the mass model is based on the work of Steinfeldt et al. [18]. such that a comparison to recent aeroassist technology studies may be performed. No mass margin is incorporated into the study.

1. *Propulsion and Reaction Control Systems*

The main component of the propulsion system mass is the propellant required for descent and landing. This value is calculated as a part of the vehicle state as shown in Eq. (1). Since there are no mass drops during the fully-propulsive trajectories analyzed in this study (a single-stage propulsive system is assumed), the propellant required by a specific trajectory is calculated by subtracting the landed mass from the vehicle's initial mass:

$$\dot{m} = \frac{T}{I_{\text{sp}} g_0} \tag{1}$$

In systems level studies, I_{sp} is generally determined through the type of fuel used. As in most previous human Mars exploration studies, the reference propellant assumed is LOX/CH_4. This choice is based largely on the ability to produce methane while on the surface of Mars and the need for commonality in the Earth–Mars and Mars–Earth transportation systems required for human exploration [4,19]. The reference case of this study assumes a constant I_{sp} of 350 s with no variation with total pressure. However, the system's sensitivity to I_{sp} is provided. The vehicle's thrust, T in Eq. (1), is assigned by the controller and is limited in magnitude by a specified thrust to Mars-weight ratio (T/W).

In the reference case, a constant-thrust gravity turn is used for the terminal segment of the EDL sequence. Gravity turns of the same ΔV require less fuel for increasing thrust levels. Theoretically, gravity turns are most efficient if employed with infinite thrust at the instant before touchdown. Figure 1 shows that a mass savings of more than 15% can be realized if full throttle is used instead of a throttle setting of 50% for a vehicle with the capability of producing a thrust of 670 kN. The difference between the masses of propulsion systems capable of producing 670 and 335 kN is modeled at approximately 500 kg for a four engine configuration using Eq. (2). Therefore, propulsion system mass sizing is not performed in this example. Note that, in this investigation, propellant mass fraction (PMF) is defined as the total propellant mass divided by the total initial vehicle mass. These results are specific to the T/W and I_{sp} of the vehicle, however, they reflect the significant losses that can be incurred by lower thrust maneuvers.

As such, in this investigation, the terminal gravity turn maneuvers use the maximum allowable thrust set by a wet vehicle thrust-to-weight ratio. The assigned thrust-to-weight ratio is based on the initial weight of the vehicle at Mars. The thrust is determined through this manner so that engine capability is scaled with the size of the vehicle. Previous studies have used T/W ratios ranging from two to five [19]. The reference case in this study uses a T/W of three as a compromise between performance and engine size. The sensitivity to this parameter is explored later.

In modeling the mass of the engines, it is necessary to specify the quantity of engines required and the mass of each engine. Individual engines are scaled according to the following relationship:

$$m_{\text{engine}} = 0.00144T + 49.6 \tag{2}$$

where T is the engine thrust in N and m_{engine} is the engine mass in kg. The relationship was developed by Christian et al. through regression analysis of data for conceptual LOX/CH_4 engines [19]. The upper bound of the thrust of the engines used in forming the relationship was 200 kN [20]. In determining the mass of the engines for the current study, the thrust produced by a single engine is limited to this value. Limiting the maximum thrust that a single engine can produce and specifying the required total thrust of the propulsion system dictates the minimum number of engines on the vehicle. However, more consideration of the number and placement of engines is necessary.

It has been shown that individual engines placed in the center of the body can effectively eliminate the drag of the vehicle; whereas, placing engines at the periphery of the vehicle can preserve the vehicle's aerodynamic drag for thrust coefficients [defined in Eq. (3)] lower than one [21]:

$$C_T = \frac{T}{\bar{q}A} \tag{3}$$

In an effort to model the aeropropulsive effects, a drag coefficient multiplier is defined through the linear piecewise function presented in Eq. (4). The model was developed using wind-tunnel test data for a 60° sphere-cone with a peripheral retropropulsion configuration of three engines thrusting into a Mach 2 freestream [22]. The model reflects preservation of drag for thrust coefficients lower than one, degraded drag between thrust coefficient values of one and three, and complete elimination of drag with thrust coefficient values greater than three. The system's sensitivity to aeropropulsive effects is revisited later in this paper:

$$k_{C_D} = \begin{cases} 1 - 0.0849C_T & C_T \le 1.036 \\ 1.866 - 0.921C_T & 1.036 < C_T \le 1.643 \\ 0.78 - 0.26C_T & 1.643 < C_T \le 3 \\ 0 & 3 < C_T \end{cases} \tag{4}$$

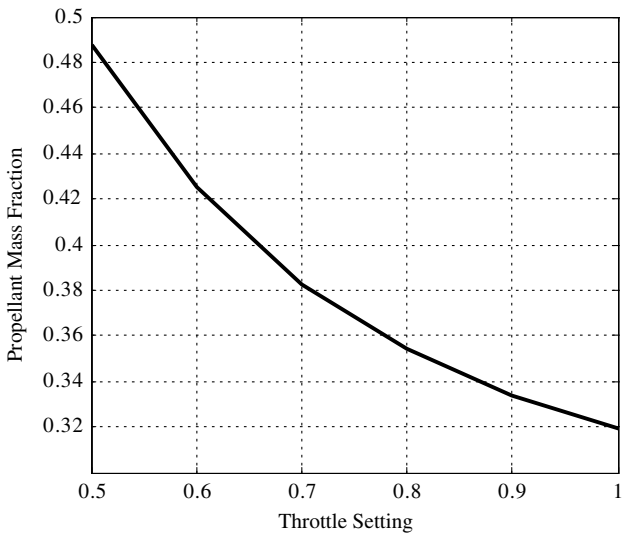

Fig. 1 PMF of a terminal gravity turn performed at various throttle settings for a 60 mT, 10 m-diam vehicle.

Assuming sufficient throttling authority, additional engines also allow for engine-out capabilities thus increasing the system reliability. For these reasons as well as the aerodynamic benefits, the vehicles in this study have no less than four engines situated on the periphery of the vehicle's body.

Because of the heavy reliance on propulsion for deceleration in the current EDL architecture, the mass of the vehicle's propellant tanks is significant. For this study, the propellant tanks are sized according to the volume of propellant needed for the trajectory. An oxidizer to fuel ratio of 3.5 is assumed with the density of the methane and liquid oxygen to be 422.6 and 1140.1 kg/m^3 respectively. Titanium tanks are assumed with an operating pressure of 1.4 MPa [23]. The mass of cryogenic coolers is not modeled in this study.

Throughout the entry trajectory, it is assumed that attitude control is performed by a RCS. The mass of the RCS hardware is modeled as 0.5% of the vehicle's initial mass. The RCS propellant mass is calculated based on a ΔV requirement of 30 m/s and an RCS I_{sp} of 200 s. This method of modeling is consistent with previous high-mass Mars conceptual studies [18,19].

2. *Structure*

To capture trajectory effects on the vehicle's structural mass, a relationship based on peak dynamic pressure was used to size the forebody's underlying structure. The relationship was formulated through regression analysis of previous robotic and human entry missions and is provided in Eq. (5):

$$m_{\text{FBS}} = m_0 \cdot 0.0232(\bar{q}_{\max})^{0.1708} \tag{5}$$

Referencing historical and conceptual robotic and crewed vehicles, Steinfeldt et al. [17,18] estimated the backshell mass as 14% of the vehicle's initial mass. The current study models backshell mass in the same manner. The backshell protects the leeward surface of the vehicle from debris and heating during entry. The vehicles used in Steinfeldt et al.'s model experienced much higher heat rates than those encountered in the current study, and therefore, the backshell mass estimation is considered very conservative. The system's sensitivity to the backshell mass is examined later in this paper. The forebody structure and backshell are combined to provide the vehicle's total structural mass.

3. *Thermal Protection Systems*

During atmospheric entry, heating of the vehicle is a concern. Because the velocities experienced in this study are below 6 km/s, radiative heating is neglected [24]. Aerothermodynamic heating is modeled using the Sutton–Graves stagnation point convective heating equation [25]:

$$\dot{q}_{\text{conv}} = k\sqrt{\frac{\rho}{r_n}} \cdot v_{\text{rel}}^3 \tag{6}$$

In Eq. (6), r_n is the effective nose radius of the vehicle and is approximated as a quarter of the vehicle's diameter for this study. The constant, k, depends on the composition of the Martian atmosphere and is $1.9027\text{e}-8\ \text{kg}^{1/2}/\text{cm}^2$.

Vehicle heating is generally mitigated with the use of an ablative TPS. The vehicle's TPS mass is estimated by the regression model based on the total heat load provided in Eq. (7) [26]:

$$m_{\text{TPS}} = m_0 \cdot 0.091(q_{\text{conv,total}})^{0.51575} \tag{7}$$

4. *Payload*

Applying the preceding definitions, the payload of the spacecraft is defined as the mass remaining once the preceding system masses are subtracted from the vehicle's landed mass. Systems not address in the previous modeling including life support, guidance and navigation, communications, and cryogenic coolers are neglected for mass modeling purposes:

$$m_{\text{payload}} = m_{\text{landed}} - (m_{\text{prop sys}} + m_{\text{RCS sys}} + m_{\text{FBS}} + m_{\text{backshell}} + m_{\text{TPS}}) \tag{8}$$

C. Reference Mission

The current study considers two entry options: direct entry from a hyperbolic approach trajectory and entry from orbit as depicted in Fig. 2. In the direct entry case, the simulation is initiated at a 400 km altitude with an inertial velocity of 5.85 km/s, a state that is equivalent to 6 km/s at atmospheric interface (altitude of 125 km). The initial FPA of the vehicle is optimized with respect to the mission's overall PMF. In the entry-from orbit cases, the vehicle is initially assumed to be in a 400 km altitude circular orbit (inertial velocity of 3.36 km/s). The vehicle performs a deorbit maneuver to change its velocity and FPA. Once again, the magnitude of the deorbit burn is optimized with respect to overall PMF. Once the spacecraft has begun its descent sequence, there are no deployments, separations, or changes in configuration. The vehicle follows a ballistic trajectory, relying only on propulsion and drag for

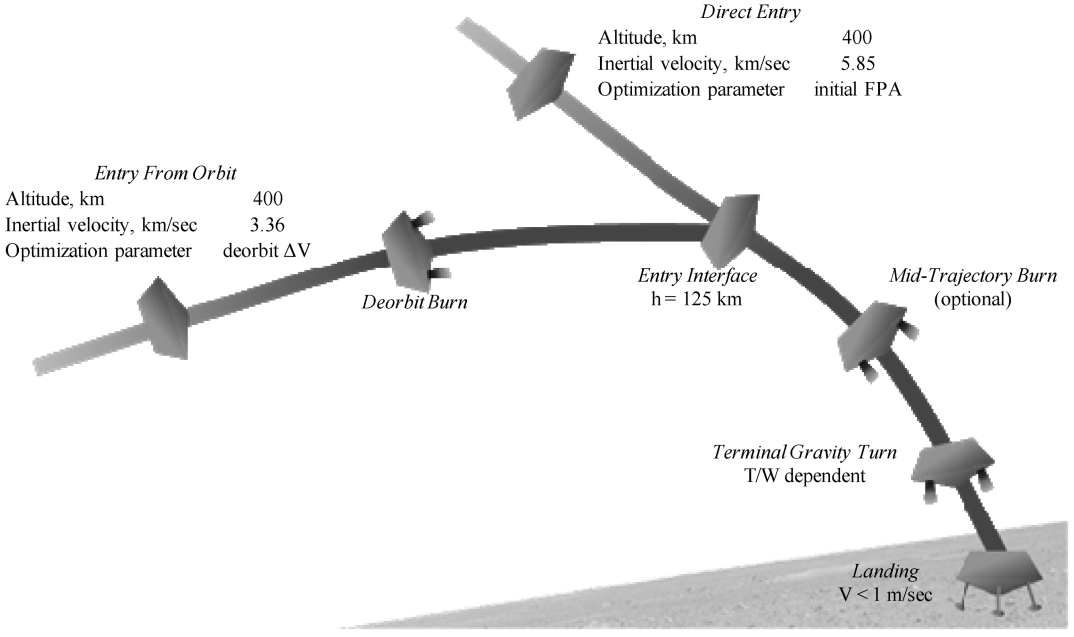

Fig. 2 Fully-propulsive EDL sequence of events.

deceleration. All trajectories end with a constant-thrust gravity turn that is performed at maximum thrust and initiated at a time consistent with the vehicle T/W. The reference trajectory deceleration is performed through only aerodynamic drag and this terminal gravity turn maneuver.

Throughout the EDL sequence, there are various constraints that must be satisfied. First, the landing conditions must be met. To ensure a soft landing, a Newton-based solver is used to calculate the altitude of the initiation of the terminal deceleration phase, dependent on the vehicle's T/W. During terminal descent, the constant-thrust gravity turn is employed to arrive at the targeted surface elevation within 1 m and at less than 0.01 m/s. In the reference trajectory, no additional ΔV is provided for a constant velocity, vertical descent segment, divert maneuver, or precision propulsive guidance phase that may ultimately be required. A maximum g-limit constraint is also placed on the trajectories. Because of an expected astronaut deconditioning period on the order of six to nine months, the maximum g-load constraint is set to five Earth gs. A heat rate constraint is also placed on the trajectories to determine if the ablative TPS employed by current robotic missions can be reduced through the use of propulsion early in the trajectory. The g-limit and heat rate constraints are not implemented in the reference trajectories but are used later in this study.

III. Results

A. Reference Trajectories

As a benchmark for this investigation, reference trajectories for both the direct entry and entry-from orbit scenarios are first established. The vehicle used for these reference cases is described in Table 4. The provided mass, ballistic coefficient, and T/W are for the vehicle at the initiation of the from orbit or direct descents. Note that deceleration is accomplished without aeroassist technology elements such as lifting configurations, parachutes, or IADs.

Table 4 Baseline vehicle parameters

Parameter	Value
Initial mass, mT	60
Vehicle diameter, m	10
Ballistic coefficient, kg/m^2	477.5
Initial T/W	3
I_{sp}, s	350

Table 5 Events and parameters of the reference trajectories

Event/parameter	From orbit	Direct
Event		
Simulation initiation		
Time, s	−2176	−167
Altitude, km	400	400
Relative velocity, km/s	3.091	5.601
Relative FPA, deg	0.00	-21.99
Entry interface		
Time, s	0	0
Altitude, km	125	125
Relative velocity, km/s	3.28	5.76
Relative FPA, deg	−2.92	−11.49
Gravity turn initiation		
Time, s	740	295
Altitude, km	24.3	19.1
Relative velocity, km/s	2.390	1.987
Relative FPA, deg	−4.18	−3.27
Trajectory termination		
Time, s	878	424
Altitude, km	0	0
Relative velocity, km/s	0	0
Relative FPA, deg	−84.61	−86.25
Parameter		
Peak heat rate, W/cm^2	7.66	48.89
Total heat load, J/cm^2	2108	5837
Peak-g load (Earth gs	2.17	2.92
Peak dynamic pressure, Pa	5490	13,608
Propellant mass fraction, %	47.65	41.95
Payload mass fraction, %	14.66	16.00

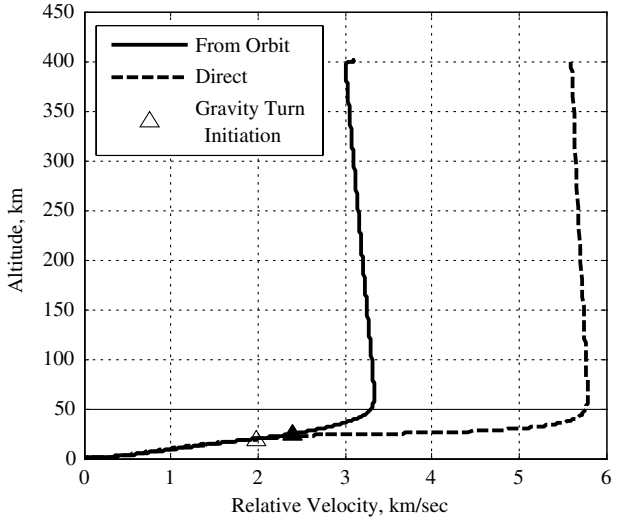

Fig. 3 Reference trajectories.

The entry-from-orbit reference case uses the mass-optimum deorbit ΔV, while the direct entry reference case begins with the mass-optimum initial FPA. At the end of each of these trajectories, a constant-thrust terminal gravity turn is used to ensure a safe landing. For the majority of the descent, the vehicle is not thrusting. The reference trajectories are outlined in Table 5 and Fig. 3. No in-flight constraints are considered in these two reference cases. Therefore, the mass optimization finds an initial state of the vehicle which maximizes drag throughout the trajectory. This strategy minimizes the ΔV required by the terminal gravity turn. Note that for the direct entry case, the peak heat rate is relatively significant, requiring use of a TPS.

B. Addition of Heat Rate Constraint

This aspect of the investigation explores the possibility of reducing or eliminating the entry system TPS by flying a heat rate constrained trajectory. Assuming the system is in radiative equilibrium, the heat rate limit can be computed for a given structural material by assigning a maximum allowable temperature in Eq. (9):

$$\dot{q}_{\text{conv}} = k\varepsilon T^4 \tag{9}$$

In Eq. (9), T temperature of the surface of the vehicle's forebody in Kelvin, k is the Stefan–Boltzmann constant (5.67×10^{-8} W/m^{2}K^4), and ε is the emissivity of the forebody material. Assuming a maximum heat rate of 1 W/cm^2 and an emissivity of 0.8, the surface temperature of the forebody at the stagnation point is computed as approximately 415°C. This represents a significant decrease in the peak temperature relative to the 850 and 1540°C experienced by the entry-from orbit and direct entry reference trajectories, respectively. An argument can be made that the TPS may be reduced or eliminated for sufficiently low peak heat rates. Limiting the peak heat rate reduces the total heat load during the trajectory, resulting in a lower TPS mass calculated by Eq. (7). To fly a heat rate constrained trajectory, a midtrajectory burn (MTB) is included in the EDL sequence. This additional propulsive maneuver increases the vehicle's PMF. However, by slowing the vehicle at the right point in the trajectory, the peak heat rate can be drastically reduced. Therefore, it may be possible to reduce, or even eliminate, the mass, complexity, and cost of an ablative TPS with the implementation of a midtrajectory burn.

The midtrajectory propulsive maneuver was first designed as a constant-thrust burn. As with a gravity turn, the thrust was directed in the opposite direction of the velocity. An optimization of landed mass

was performed using three design variables: the altitude at which the midtrajectory burn was initiated, the burn ΔV, and the thrust magnitude of the burn. This burn was performed at constant thrust, but unlike the gravity turn, it was not necessarily performed at maximum thrust. Reducing the thrust magnitude of the midtrajectory burn allowed for longer burn times thus controlling the vehicle's velocity over an extended period of the trajectory. This proved necessary to meet lower peak heat rate constraints.

The midtrajectory burn acts to slow the vehicle before the heating constraint is violated. Not only does this maneuver require propellant, but the decrease in velocity also greatly reduces the deceleration due to drag. The vehicle drag is also reduced due to aeropropulsive effects. Example trajectories using the constant-thrust midtrajectory burn and their respective PMFs are provided in Fig. 4. For these trajectories, the midtrajectory propulsive maneuver was initiated at the 1 W/cm^2 heat rate constraint and was performed at throttle settings of 100, 75, and 50%. The length of the burn (ΔV) was specified to ensure that the heat rate constraint was not violated during the coast phase after the MTB was terminated.

As seen in Fig. 4, the more mass-optimal trajectories are those that are nearer to the constraint for longer periods of time. There are three reasons for this. First, midtrajectory burns with lower throttle settings require less ΔV during this segment of the trajectory. This is the result of terminating the MTB at a lower altitude. Upon termination, the vehicle has less altitude to accelerate and therefore less velocity to remove during the terminal gravity turn maneuver. Second, trajectories closer to the constraint experience more drag. At every altitude (or density), the vehicle is at a higher velocity resulting in a larger drag force. Finally, lower throttle settings experience less aeropropulsive drag degradation. The lower throttle settings reduce thrust coefficient resulting in drag coefficient multipliers closer to one as calculated in Eq. (4). For the preceding reasons, it is advantageous to develop a control algorithm that uses the minimum thrust level required to meet the heat rate constraint resulting in a heat rate-riding portion of the trajectory. This requires a variable thrust (throttling) method for the midtrajectory burn.

C. Midtrajectory Propulsive Maneuver Control Law with Variable Thrust

Assuming knowledge of the vehicle's altitude at all times during the trajectory and an accurate model of the Mars atmosphere, the desired velocity of the spacecraft during the midtrajectory burn can be calculated by rearranging the Sutton–Graves stagnation point convective heating equation into the form shown in Eq. (6). Because of the previous optimality argument, defining the heat rate constraint defines the preferred trajectory of the vehicle during this phase of flight:

$$v_{\text{rel,con}} = \left(\frac{\dot{q}_{\text{conv}} \sqrt{\frac{r_n}{\rho}}}{k} \right)^{1/3} \tag{10}$$

Assuming that the thrust and drag forces dominate during propulsive maneuvers, the time derivative of the spacecraft velocity can be estimated through Eq. (11) where T and D are the thrust and drag forces:

$$\frac{\mathbf{dv_{rel}}}{\mathrm{d}t} = \frac{\mathbf{T} + \mathbf{D}}{m} \tag{11}$$

During the midtrajectory burn maneuver, thrust and drag are directed in the opposite direction of the velocity vector, allowing for a simplification of the thrust and drag vectors in Eq. (8). Through discretization, Eq. (12) can be formulated from Eq. (11):

$$\Delta \mathbf{v}_{\text{rel}} = -\Delta t \frac{T + D}{m} \hat{v}_{\text{rel}} \tag{12}$$

In Eq. (12), Δv_{rel} is defined as the difference between the actual relative velocity and the desired relative velocity with respect to the heat rate constraint. The Δv_{rel} term can be thought of as the necessary change in velocity to place the vehicle on the heating constraint:

$$\Delta \mathbf{v}_{\text{rel}} = \mathbf{v}_{\text{rel}} - \mathbf{v}_{\text{rel,con}} \tag{13}$$

Substituting into Eq. (12), discretizing, and solving for thrust gives the following control law:

$$T(t_k) = -\left(\frac{m(t_{k-1})(v_{\text{rel}}(t_{k-1}) - v_{\text{rel,con}}(t_{k-1}))}{t_k - t_{k-1}} - D(t_{k-1}) \right) \hat{v}_{\text{rel}}(t_{k-1}) \tag{14}$$

Because of its dependence on information from the previous time step, the preceding described controller lags the system; the thrust calculated is that necessary to correct the velocity of the previous time step. However, with a sufficiently small time step, the lag of the controller is negligible and the spacecraft closely follows the contour provided by the heat rate constraint.

With the variable thrust control law, the entry-from orbit and direct entry reference trajectories are resimulated with an assumed peak heat rate constraint of 1 W/cm^2. As shown in Fig. 5 and Table 6, both trajectories ride the heat rate constraint for a considerable portion of the descent. When mass sizing is performed on the direct entry case,

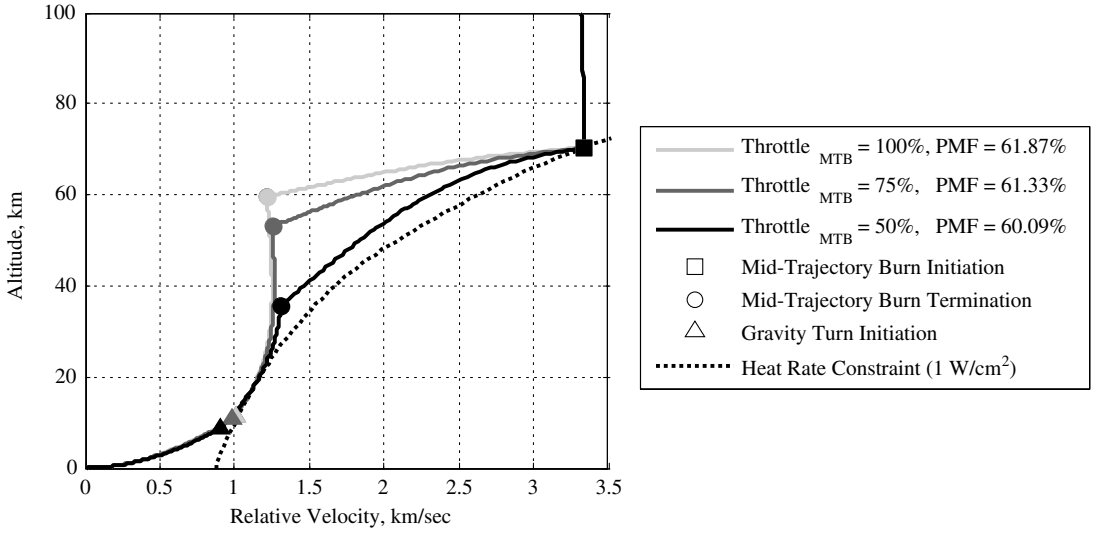

Fig. 4 Trajectories using a constant-thrust midtrajectory burn.

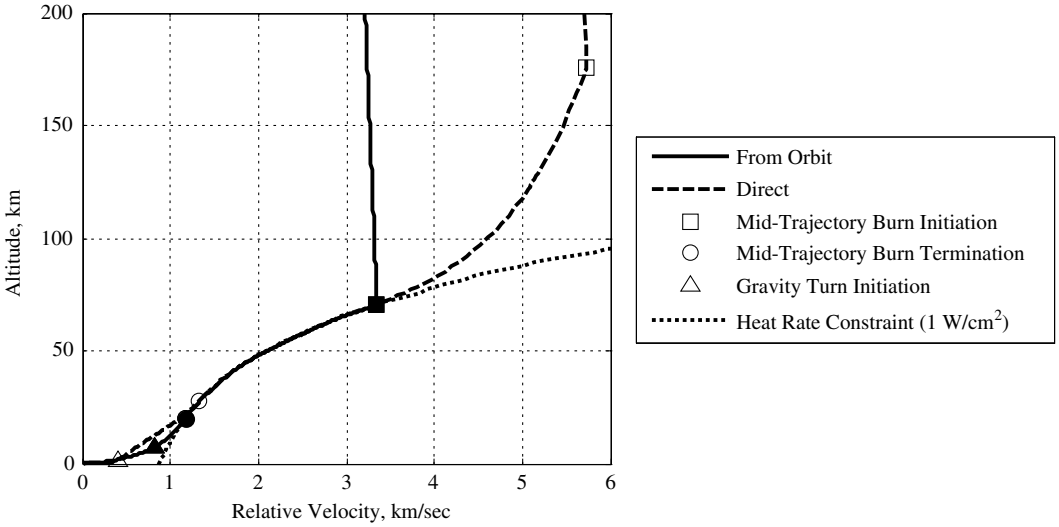

Fig. 5 Baseline vehicle employing a variable-thrust midtrajectory burn.

the combined mass of the supporting systems and required propellant are greater than the initial mass, thus resulting in a negative payload mass fraction. Therefore, due to the large PMF (nearly 76%), the direct entry case is deemed infeasible.

While the entry-from orbit case is able to begin the midtrajectory burn when the vehicle reaches the heat rate constraint, the direct entry must begin the burn exoatmospherically. Because of the increased velocity of the direct entry, the vehicle would reach the heat rate constraint along a much flatter region of the constraint. As the constraint becomes more horizontal (i.e. at higher velocities), greater changes in velocity are required for the same change in altitude. To meet the constraint, the vehicle needs to increase thrust or direct its thrust in the vertical direction. (Lift may be used for this purpose, but it is not applied in this study. Incorporation of lift is considered future work.) For this study, the thrust magnitude is limited by a specified T/W, and the direction of thrust is always defined in the opposite direction of the vehicle's velocity. The remaining option for meeting the heat rate constraint for high velocity cases is starting the midtrajectory burn earlier in the trajectory. This allows for decreases in velocity before reaching denser regions of the atmosphere where sufficient heating occurs. The portion of the midtrajectory burn executed prior to reaching the heat rate constraint is performed at maximum thrust to limit losses. Within the simulation, the altitude at which to begin this burn is explicitly calculated so that the resulting vehicle trajectory is tangent to the heat rate constraint when the two intersect. At this point, the thrust is throttled according to the control law provided by Eq. (14). After some time riding the heat rate constraint, drag provides enough deceleration so that thrust is no longer required to meet the constraint. In many trajectories, this results in a period of no thrust between the midtrajectory burn and the final gravity turn maneuver. As shown in Table 6 for the case of a 1 W/cm^2 constraint, this nonthrusting phase of flight spans a relatively small range of altitudes. These behaviors are shown in Figs. 5 and 6.

D. Mass Sizing

To study the impact of a fully-propulsive descent on mission capability, the payload mass fraction is calculated using the sizing methodology outlined earlier in this report. For comparison, the mass breakdowns of the baseline vehicle for the reference trajectory from orbit as well as the fully-propulsive descent with a heat rate constraint of 1 W/cm^2 are provided in Table 7. As expected, the fully-propulsive descent system sees a significant increase in necessary propellant. The added propellant requires larger propellant tanks resulting in additional mass growth. In this case, the mass benefit of reducing the TPS mass is overshadowed by the increase in propellant and propellant tank mass, resulting in a drastically lower payload mass fraction.

E. Sensitivity Analysis

To identify and further understand the key parameters of a fully-propulsive EDL sequence, sensitivity analysis was performed. This aspect of the analysis investigated the impact of propulsive system performance, aeropropulsive effects, structure models, initial mass, and heat rate limit on payload delivered to the surface of Mars.

Table 6 Events and parameters of trajectories employing midtrajectory burns

Event/parameter	From orbit	Direct
Event		
Simulation initiation		
Time, s	−2448	−193
Altitude, km	400	400
Relative velocity, km/s	3.091	5.599
Relative FPA, deg	0.00	−20.68
Entry interface		
Time, s	0	0
Altitude, km	125	125
Relative velocity, km/s	3.291	5.123
Relative FPA, deg	−2.15	−8.84
Midtrajectory burn initiation		
Time, s	664	−52
Altitude, km	70.4	175.5
Relative velocity, km/s	3.340	5.723
Relative FPA, deg	−0.61	−11.91
Midtrajectory burn termination		
Time, s	1043	255
Altitude, km	20.4	27.6
Relative velocity, km/s	1.173	1.323
Relative FPA, deg	−16.21	−14.20
Gravity turn initiation		
Time, s	1082	345
Altitude, km	7.2	1.2
Relative velocity, km/s	0.830	0.399
Relative FPA, deg	−23.04	−35.27
Trajectory termination		
Time, s	1119	355
Altitude, km	0	0
Relative velocity, km/s	0	0
Relative FPA, deg	−80.38	−70.72
Parameter		
Peak heat rate, W/cm^2	1.00	1.00
Total heat load, J/cm^2	646	251
Peak-g load (Earth gs	2.84	4.71
Peak dynamic pressure, Pa	2951	1804
Propellant mass fraction, %	59.95	75.86
Payload mass fraction, %	4.25	−11.58

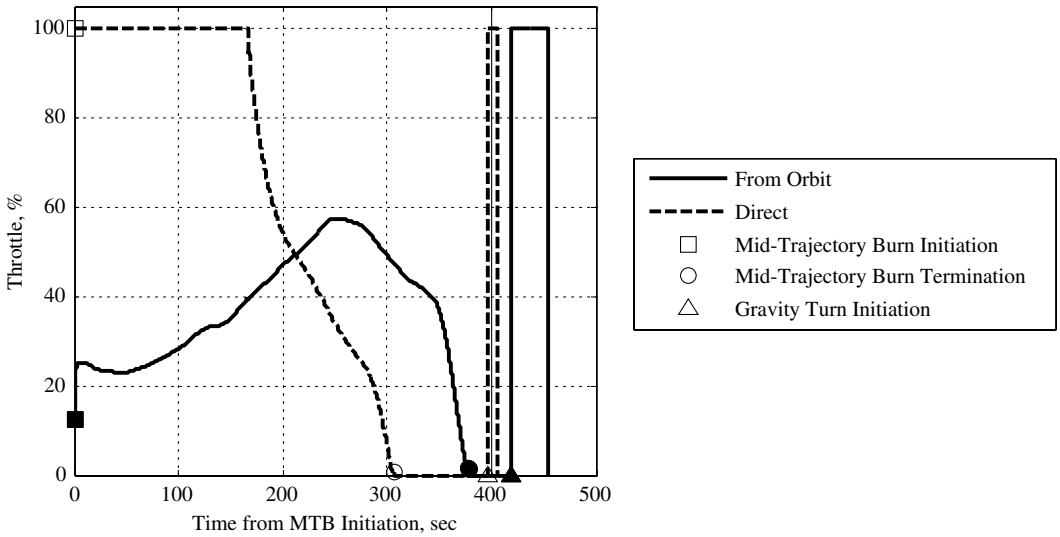

Fig. 6 Control history for the baseline vehicle employing a variable-thrust midtrajectory burn.

1. Propulsion Performance

To investigate the sensitivity of payload mass to propulsive system performance, the vehicle's thrust-to-weight ratio and specific impulse are varied from 2 to 10 and 250 to 1250 s, respectively. The analysis was performed on the baseline vehicle using a variable thrust midtrajectory burn with a heat rate constraint of 1 W/cm^2.

Contrary to the results shown in Fig. 1, the vehicle's thrust-to-weight ratio has negligible impact on the overall PMF for heat rate limited entries, since the midtrajectory burn is not generally performed at maximum thrust. In the trajectories computed, the midtrajectory burn ΔV is approximately three times as large as the terminal gravity turn ΔV. Therefore, the benefit of having a larger maximum thrust available is not fully realized. Note that improvements in vehicle T/W do not enable heat rate constrained direct entries.

Further exploration of the data shows that bounds can be set on the required T/W based on the heat rate and g-load constraints. The heat rate constraint defines the lower boundary of the thrust-to-weight ratio. In the current control structure, the vehicle must have the ability to travel along the heat rate constraint for a significant portion of the trajectory. For the constraints and trajectories examined in this study, the lower bound on the required T/W can be approximated as 2.5. For lower thrust-to-weight ratios, the midtrajectory burn must be started earlier in the trajectory resulting in higher propellant needs. The upper bound of the vehicle's thrust-to-weight is determined by the allowable g-load constraint. For five Earth gs, the maximum Mars thrust-to-weight ratio can be calculated as approximately 13. However, use of maximum thrust at this T/W would result in breaching the g-load constraint due to additional deceleration due to drag (maximum of 1.5 gs for the cases examined in this study). As such, a conservative maximum T/W on the order of 10 is appropriate. The optimum shown in Fig. 7 occurs at a T/W of five. The optimum occurs as a result of balancing the increased efficiency of higher thrust burns and the increased engine mass necessary for that higher thrust.

Table 7 Mass breakdown of the baseline vehicle for the entry-from-orbit case

System	Percent of initial mass	
	Reference trajectory, 7.66 W/cm^2	Fully-propulsive, 1 W/cm^2
Propulsion system	56.53	70.11
Propellant	47.65	59.95
Engines	1.94	1.94
Propellant tanks	4.93	6.20
RCS hardware	0.50	0.50
RCS propellant	1.52	1.52
Structure	24.10	23.08
Forebody	10.10	9.08
Backshell	14.00	14.00
TPS	4.71	2.56
Payload	14.66	4.25

Unlike thrust-to-weight ratio, the vehicle's specific impulse has significant impact on the overall PMF and, consequently, delivered payload. The range of specific impulses included in this study is expanded beyond the current technological limits to include advanced propulsion systems such as nuclear thermal rockets. As can be seen in Fig. 7, increasing I_{sp} greatly impacts payload mass fraction. The previously infeasible direct entry is enabled once the I_{sp} becomes greater than 520 s. Note that for specific impulses of 490 and 860 s, respectively, the entry-from orbit and direct entry cases deliver equivalent payload as the reference trajectories (see Table 5).

2. Aeropropulsive Effects and Structural Modeling

In an effort to examine the impact of the aeropropulsive effects and structural modeling on delivered payload, a study was conducted in which the baseline models were altered. The aeropropulsive effect model given in Eq. (4) was replaced with a simple percent multiplier. As shown in Fig. 8, the baseline vehicle entering from orbit retains approximately 50% of its overall drag during propulsive maneuvers. Also, the vehicle must conserve at least 15% of its drag to remain feasible. From the analysis, it is seen that, for the fully-propulsive descent architecture, the development of retropropulsion configurations which maintain drag could lead to increases in delivered payload on the order of 5% of the vehicle's original mass. To examine the impacts of structural modeling, the mass fraction assigned to backshell mass was changed. As can be seen in Fig. 8, reductions in structural mass fraction directly translate to higher payload mass fractions. Unfortunately, retropropulsion configurations and lightweight structures by themselves do not enable direct entries.

3. Initial Mass and Heat Rate Constraint

To further examine the sensitivity to the heat rate constraint, a series of cases were simulated. These cases included heat rate constraints ranging from 0.1 to 10 W/cm^2 and initial masses spanning 20 to 100 mT. The results of this study are presented in Fig. 9 for both entry-from orbit cases and direct entry cases. As seen in this figure, the payload mass fraction increases as the heat rate constraint is relaxed. This is expected as a higher heat rate constraint allows for more deceleration due to drag and, therefore, less propellant use throughout the trajectory. Because of the required TPS mass for higher heat rates, there is a region of cases (heat rate constraints of 2–3 W/cm^2, initial masses greater than 80 mT) which are outperformed by lower heat rate trajectories. This result suggests

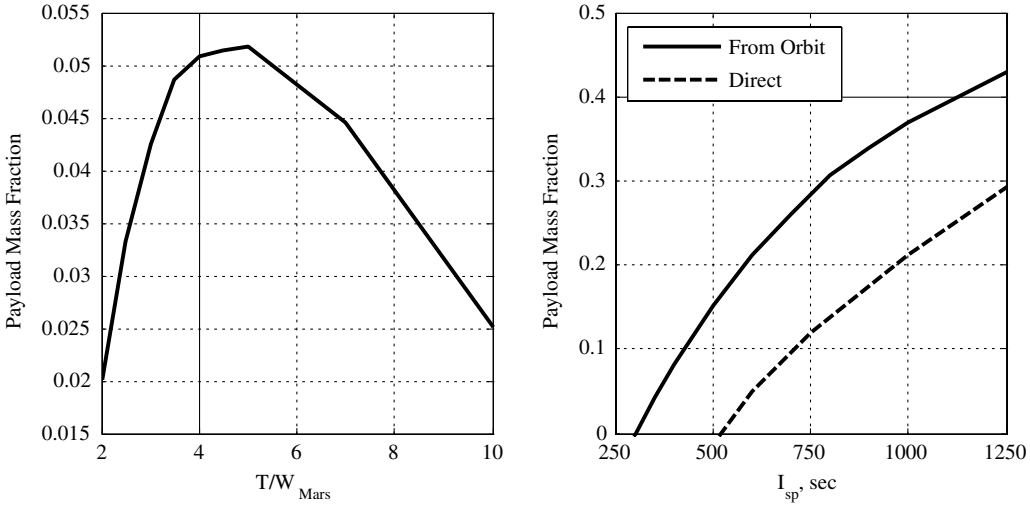

Fig. 7 Propulsion system capability sensitivity analysis.

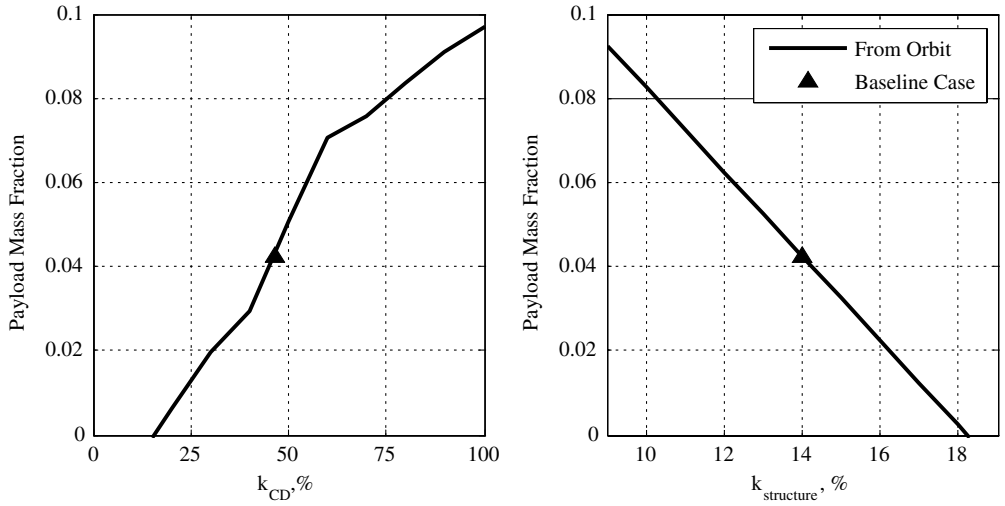

Fig. 8 Aeropropulsive effects and structural modeling sensitivity analysis.

that, for these cases, using propulsion to only mitigate and not eliminate heating concerns is inefficient. Figure 9 also shows the tendency to limit the magnitude of the midtrajectory burn through the initial trajectory optimization. The extreme of this trend is shown as the 5, 7, and 10 W/cm^2 contours merge as the initial mass decreases. These trajectories require no midtrajectory burn to adhere to the heat rate constraint, and therefore, fly trajectories similar to that of the reference case.

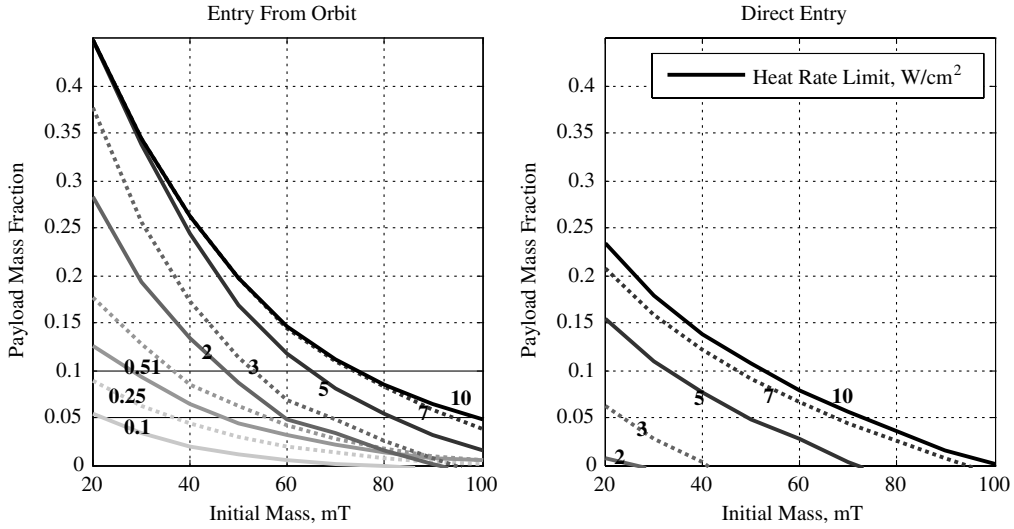

Fig. 9 Initial mass and heat rate constraint sensitivity analysis.

Table 8 Comparison of aeroassist and fully-propulsive EDL systems

Parameter	Fully-propulsive descent (from orbit) 1 W/cm^2	5 W/cm^2	7 W/cm^2	CUIP [18] (lifting, IAD)	DRM 3.0 [27] (aerocapture, parachutes)
Peak heat rate, W/cm^2	1.00	5.00	7.00	19.18	——
Total heat load, J/cm^2	646	2791	2293	5018	——
Peak-g load (Earth gs	2.84	2.26	2.18	7.88	——
Peak dynamic pressure, Pa	2951	5009	5265	49,996	——
Propellant mass fraction, %	59.95	49.70	47.74	10.62	18.72
Payload mass fraction, %	4.25	11.82	14.42	43.23	50.88

Beyond the sensitivity to the heat rate constraint, Fig. 9 shows the feasibility limits of the current fully-propulsive descent architecture. Cases are deemed infeasible if the mass sizing algorithm assigns a negative payload mass fraction. In the scope of the study presented here, the entry-from orbit cases become infeasible for the 100 mT cases which have heat rate constraints below 3 W/cm^2. The direct entry cases are considerably more difficult and therefore result in many more failed cases. As seen in Fig. 9, all direct entry cases with heat rate constraints less than 2 W/cm^2 are infeasible. By comparing the two plots, it can be seen that a direct entry's payload mass fraction is approximately 15–30% less than a corresponding entry-from orbit case. The fact that fully-propulsive descent strategies are best implemented from orbit is well aligned with high-mass Mars exploration architectural options that baseline advanced in-space propulsion (as opposed to aeroassist technology) for the Mars arrival maneuver.

F. Comparison with Aeroassist Entry, Descent, and Landing Systems

Table 8 compares the fully-propulsive descent architecture against a more traditional aeroassist EDL system. As expected, the fully-propulsive descent recognizes significant decreases in peak heat rate, total heat load, and peak dynamic pressure at the expense of propellant and subsequently payload. The suggested 1 W/cm^2 heat rate constrained case is greatly outperformed by the aeroassist system. However, by easing the constraint to 5 or 7 W/cm^2, the gap in performance is narrowed somewhat. In this comparison an I_{sp} of 350 s is assumed. As seen in Table 8, the fully-propulsive descent requires some form of technology advancement (see Fig. 7) to become competitive with traditional aeroassist strategies.

G. Mission Impact

Introduction of the fully-propulsive descent can significantly impact the dynamics and requirements of the EDL segment from a mission architecture, complexity, and reliability perspective.

1. *Mission Architecture*

Implementing a fully-propulsive descent during the EDL segment of a mission will impact the overall mission architecture. From the preceding analysis, a heat rate limited direct entry requires a large PMF which significantly decreases or eliminates the payload delivered to the Mars surface. As shown in this investigation, fully-propulsive descents are best implemented from orbit. Once entry-from orbit is selected, an appropriate method for orbit insertion must be determined. Because of the availability of a capable propulsion system, propulsive orbital insertion is likely. The propulsive maneuver to transfer the vehicle from the hyperbolic approach to the 400 km altitude circular orbit requires a ΔV of approximately 2.5 km/s. This results in a PMF on the order of 50% for the orbit insertion burn (assuming an I_{sp} of 350 s). If all of the needed propellant is to be transported from Earth, the baseline vehicle with a mass of 60 mT in Mars orbit grows to over 350 mT at Earth-departure. However, an in-situ supplied propellant depot in Mars orbit would allow a mission architecture in which the spacecraft refuels after insertion into Mars orbit [28]. Also, significant improvements in Earth-launch mass can be realized if propellant depots are also available in low Earth orbit. Figure 10 outlines the mass of the vehicle from Earth-launch to Mars EDL initiation and the resultant landed payload. The architecture assumes propellant resources in both Earth and Mars orbits, zero boil off, and that both the Earth-departure burn and Mars orbital insertion burn are performed by the vehicle. This mission architecture requires a 25 mT launch mass to land 2.55 or 8.65 mT of payload on the surface of Mars for fully-propulsive EDL sequences that have 1 and 7 W/cm^2 heat rate constraints, respectively, (assuming an I_{sp} of 350 s). In the same architecture, an I_{sp} of 600 s increases the payload landed on the surface of Mars to 12.67 and 15.29 mT for the same heat rate constraints.

Another orbit insertion option at Mars is aerocapture. This maneuver has been suggested by many authors including Christian et al. [19]. A similar orbit insertion maneuver is possible for the current study. If paired with refueling at Mars, the fully-propulsive descent allows for a much lower mass aerocapture system (a baseline vehicle with a mass of approximately 25 mT). After the aerocapture maneuver, the vehicle can rendezvous with the propellant depot and take on the fuel needed for the fully-propulsive descent. Because of the addition of a heat shield needed for aerocapture, this orbit insertion method increases the launch mass required. However, aerocapture greatly decreases the amount of propellant used in Mars orbital insertion and Earth-departure.

Although not examined in this study, a fully-propulsive descent allows for more flexibility in the shape of the vehicle. This in turn lets the vehicle be designed for surface operations instead of survival of EDL. The vehicle can be designed with a larger habitable volume, easier entry and egress systems, or compatibility with prepositioned surface assets. The increased functionality of the vehicle may lead to a simpler and more productive surface operations phase.

2. *Complexity*

To analyze the effect of a fully-propulsive descent on the complexity of a mission, it is appropriate to analyze both hardware

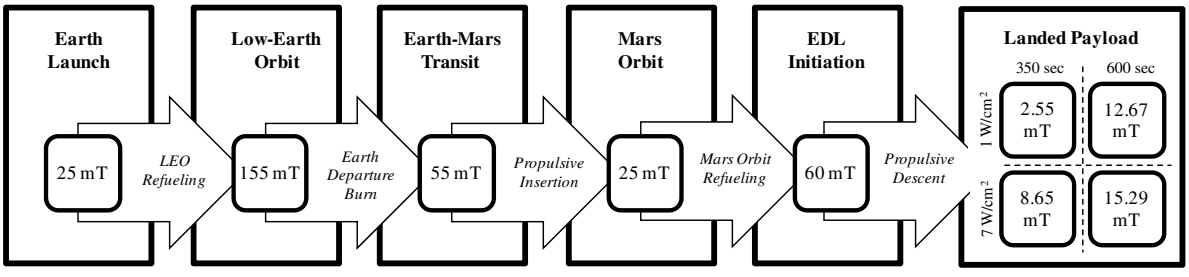

Fig. 10 Fully-propulsive EDL mission architecture.

and operations. As offered in this study, a fully-propulsive descent may be used to avoid harsh heating environments usually encountered in atmospheric transit. In this light, the difficulty of developing and employing an enhanced propulsion system is being traded for that of TPS. The performance of the propulsion system greatly impacts the feasibility of the proposed EDL sequence. The specific impulse of 350 s assumed in this study is widely accepted for LOX/CH_4 engines, and the thrust assumed for the baseline vehicle is approximately 700 kN (less than half of the thrust produced from one of the space shuttle's main engines). Throttling authority allows for added control of the vehicle and enables the heat rate limited trajectories which allow elimination of the TPS. However, throttling of high-performance rocket engines is not easily achieved. The continuous throttling ability assumed in this study would likely be implemented as a series of discrete throttle settings at a small cost to performance.

Other concerns of the fully-propulsive descent sequence include local heating in the vicinity of exposed engines and thrusting into a hypersonic flow. Research focused on supersonic retropropulsion has examined thrusting into flows with Mach numbers up to six [21], however, thrusting into flows with Mach numbers of up to 25 was assumed in this study.

The difficulties of a fully-propulsive descent must be compared against those of a more traditional EDL sequence which relies on aeroassist technology. One driver of complexity in an aeroassist trajectory is the reconfiguration of the vehicle during descent. These events often include the separation of the heat shield and backshell, deployment of a parachute or IAD, possible banking maneuvers for lifting trajectories, the use of novel aeroshell geometries for improved aerodynamic control authority, and a terminal thrusting maneuver. During an aeroassist trajectory, certain flight conditions must be met in order to successfully complete each of these events. For instance, a parachute or IAD must be deployed within a specific Mach and altitude envelope. These requirements are not present for a fully-propulsive descent.

Another source of complexity for an aeroassist trajectory is the development of the vehicle's TPS. This issue becomes increasingly difficult as the vehicle grows in size. Growth of the vehicle leads to paneling or tiling of the TPS material. Because of the limits in the size of individual panels or tiles, the quantity of the pieces needed to properly protect the vehicle increases as well as the number of seams between those pieces. This leads to increased risk and complexity as the vehicle becomes larger.

3. *Reliability*

Reliability of a fully-propulsive descent can also be compared against aeroassist EDL sequences. Of major concern would be the ability to initiate a large rocket engine after being dormant for a six to nine month transit period. This issue is present for many robotic deep space missions and is generally solved by focusing on engine reliability. However, the pressure-fed hypergolic engines typical to deep space missions are much less complex than the pump-fed, high-performance engines suggested by this study.

An increase in reliability of the fully-propulsive descent can also be realized if a divert capability is included in the EDL sequence. Divert maneuvers could be used during EDL to increase landing reliability by providing the ability to reach multiple landing sites [29]. Diverting requires propulsive maneuvers at the end of a trajectory. For the case of an aeroassist trajectory, a divert maneuver must begin after parachute or IAD separation. For a fully-propulsive descent, the divert maneuver may start at any point in the trajectory. This would increase the possible landing area thereby increasing the number of landing sites available or the range of abort-to-the-surface options.

IV. Conclusions

This study has explored the use of propulsion during the EDL sequence at Mars for high-payload missions. The study focused on replacing conventional aeroassist strategies with an architecture that relies primarily on a single-stage propulsive descent. For the study, trajectory simulation and mass sizing were performed to analyze the feasibility of a fully-propulsive descent. A heat rate boundary and associated control law were developed in an effort to limit the heating loads placed on the vehicle. The results show that the fully-propulsive descent strategy is best implemented in an entry-from orbit architecture. The fully-propulsive transit architecture provides low payload mass fractions (less than 10%) without significant improvements in I_{sp} (above the 350 s assumed), a heat rate limit in the range of 5–10 W/cm^2, or the vehicle's aeropropulsive model at high-thrust coefficients. This payload mass fraction is lower than the 20–30% payload mass fractions suggested by more traditional Mars EDL strategies. When coupled with refueling resources in Earth and Mars orbit, a fully-propulsive strategy can deliver 8.65 mT of payload to Mars with Earth-launch masses as low as 25 mT. To enable high-payload missions to Mars, conventional aeroassist strategies require further technology development in multiple areas such as thermal protection, IADs, supersonic parachutes, and aeroshell configurations. Alternatively, a fully-propulsive descent strategy would require technology advancements in high-thrust, high-I_{sp} propulsion systems, drag-preserving retropropulsion configurations, and lightweight structural materials.

Acknowledgments

The authors would like to thank the students and faculty of the Space Systems Design Laboratory at the Georgia Institute of Technology, especially Ian Clark, Michael Grant, Ashley Korzun, and Bradley Steinfeldt.

References

[1] Braun, R. D., and Manning, R. M., "Mars Exploration Entry, Descent, and Landing Challenges," *Journal of Spacecraft and Rockets*, Vol. 44, No. 2, 2007, pp. 310–323. doi:10.2514/1.25116

[2] Prakash, R., Burkhart, P. D., Chen, A., Comeaux, K. A., Guernsey, C. S.Kipp, D. M., Lorenzoni, L. V., Mendeck, G. F., Powell, R. W., Rivellini, T. P., San Martin, A. M., Sell, S. W., Steltzner, A. D., and Way, D. W., "Mars Science Laboratory Entry, Descent, and Landing System Overview," 2008 IEEE Aerospace Conference, IEEE Paper 1531, March 2008.

[3] "Vision for Space Exploration," NASA NP-2004-01-334-HQ, Feb. 2004.

[4] Drake, B. G. (ed.), "Reference Mission Version 3.0 Addendum to the Human Exploration of Mars: The Reference Mission of the NASA Mars Exploration Study Team," NASA SP-6107-ADD, June 1998.

[5] Cheatham, D. C., and Bennett, F. V., "Apollo Lunar Module Landing Strategy," Apollo Lunar Landing Symposium, NASA TM X-58006, June 1966.

[6] Cooley, C. G., and Lewis, J. G., "Viking Lander System Primary Mission Performance Report," NASA CR-145148, April 1977.

[7] Ingoldby, R. N., Michel, F. C., Flaherty, T. M., Doty, M. G., Preston, B., Villyard, K. W., and Steele, R. D., "Entry Data Analysis for Viking Landers 1 and 2," NASA CR-159388, Nov. 1976.

[8] Morrisey, D. C., "Historical Perspective: Viking Mars Lander Propulsion," *Journal of Propulsion and Power*, Vol. 8, No. 2, 1992, pp. 320–331. doi:10.2514/3.23481

[9] Spencer, D. A., Blanchard, R. C., Braun, R. D., Kallemeyn, P. H., and Thurman, S. W., "Mars Pathfinder Entry, Descent, and Landing Reconstruction," *Journal of Spacecraft and Rockets*, Vol. 36, No. 3, 1999, pp. 357–366. doi:10.2514/2.3478

[10] McGrath, D. K., and Carr, C. E., II, "Mars Pathfinder Retrograde Rocket Development," 34th AIAA/ASME/SAE/ASEE Joint Propulsion Conference and Exhibit, AIAA Paper 98-3844, July 1998.

[11] Desai, P. N., and Knocke, P. C., "Mars Exploration Rovers Entry, Descent, and Landing Trajectory Analysis," AIAA/AAS Astrodynamics Specialist Conference and Exhibit, AIAA Paper 2004-5092, Aug. 2004.

[12] Moore, C. A., and Guernsey, C., "Development and Qualification of the Rocket-Assisted Deceleration (RAD) and Transverse Impulse Rocket System (TIRS) Motors for the Mars Exploration Rover (MER)," 52nd Joint Army-Navy-NASA-Air Force (JANNAF) Propulsion Meeting, Las Vegas, NV, May 2004.

[13] Grover, M. R. III., Cichy, B. D., and Desai, P. N., "Overview of Phoenix

Entry, Descent, and Landing System Architecture," AIAA Guidance, Navigation, and Control Conference, AIAA Paper 2008-7213, Aug. 2008.

[14] Prince, J. L., Desai, P. N., Queen, E. M., and Grover, M. R., "Mars Phoenix Entry, Descent, and Landing Simulation Design and Modeling Analysis," AIAA Guidance, Navigation, and Control Conference, AIAA Paper 2008-7507, Aug. 2008.

[15] Goldstein, B., and Shotwell, R., "Phoenix: The First Mars Scout Mission (a Mid-Term Report)," 2006 IEEE Aerospace Conference, Big Sky, MT, March 2006.

[16] Powell, R. W., Striepe, S. A., Desai, P. N., and Braun, R. D., "Program to Optimize Simulated Trajectories (POST), Utilization Manual," Ver. 5.0, Sept. 1996.

[17] Steinfeldt, B. A., Grant, M. J., Matz, D. M., Braun, R. D., and Barton, G. H., "Guidance, Navigation and Control Technology System Trades for Mars Pinpoint Landing," 2008 AIAA Atmospheric Flight Mechanics Conference, AIAA Paper 2008-6216, Aug. 2008.

[18] Steinfeldt, B., Theisinger, J. E., Korzun, A. M., Clark, I. G., Grant, M. J., and Braun, R. D., "High Mass Mars Entry, Descent, and Landing Architecture Assessment," Space 2009, AIAA Paper 2009-6684, Sept. 2009 (to be published).

[19] Christian, J., Wells, G., Lafleur, J., Verges, A., and Braun, R. D., "Extension of Traditional Entry, Descent, and Landing Technologies for Human Mars Exploration," *Journal of Spacecraft and Rockets*, Vol. 45, No. 1, 2008, pp. 130–141. doi:10.2514/1.31929

[20] Klepikov, I. A., Katorgin, I. A., and Chvanov, V. K., "The New Generation of Rocket Engines, Operating by Ecologically Save Propellant 'Liquid Oxygen and Liquefied Natural Gas (Methane)'," *Acta Astronautica*, Vol. 41, Nos. 4–10, 1997, pp. 209–217. doi:10.1016/S0094-5765(98)00076-9

[21] Korzun, A. M., Cruz, J. R., and Braun, R. D., "A Survey of Supersonic Retropropulsion Technology for Mars Entry, Descent, and Landing," 2008 IEEE Aerospace Conference, IEEE Paper 1246, March 2008.

[22] Jarvinen, P. O., and Adams, R. H., "The Aerodynamic Characteristics of Large Angled Cones with Retrorockets," NASA Contract No. 7-576.

[23] Humble, R. W., Henry, G. N., and Larson, W. J., *Space Propulsion Analysis and Design*, McGraw–Hill, New York, 1995.

[24] Tauber, M. E., and Sutton, K., "Stagnation-Point Radiative Heating Relations for Earth and Mars Entries," *Journal of Spacecraft and Rockets*, Vol. 28, No. 1, 1991, pp. 40–42.

[25] Sutton, K., and Graves, R. A. Jr., "A General Stagnation-Point Convective-Heating Equation for Arbitrary Gas Mixtures," NASA TR R-376, Nov. 1971.

[26] Laub, B., and Venkatapathy, R., "Thermal Protection System Technology and Facility Needs for Demanding Future Planetary Missions," International Workshop on Planetary Probe Atmospheric Entry and Descent Trajectory Analysis and Science, Lisbon, Portugal, Oct. 2003.

[27] Drake, B. G. (ed.), "Reference Mission Version 3.0, Addendum to the Human Exploration of Mars: The Reference Mission of the NASA Mars Exploration Study Team," NASA Rept. EX13-98-036, June 1998.

[28] Grant, M. J., and Braun, R. D., "Smart Divert: A New Entry, Descent, and Landing Architecture," 47th AIAA Aerospace Sciences Meeting, Jan. 2009.

[29] Powell, J., Maise, G., and Paniagua, J., "A Self-Sustaining Earth-Mars Architecture Utilizing Martian Colonies Based on the North Polar Cap," 2001 IEEE Aerospace Conference, Big Sky, MT, March 2001.

J. Martin
Associate Editor